

# A DISCONTINUOUS GALERKIN METHOD FOR SHOCK CAPTURING USING A MIXED HIGH-ORDER AND SUB-GRID LOW-ORDER APPROXIMATION SPACE

PER-OLOF PERSSON, BENJAMIN STAMM

**Abstract.** This article considers a new discretization scheme for conservation laws. The discretization setting is based on a discontinuous Galerkin scheme in combination with an approximation space that contains high-order polynomial modes as well as piece-wise constant modes on a sub-grid. The high-order modes can continuously be suppressed with a penalty function that is based on a sensor which is intertwined with the approximation space. Numerical tests finally illustrate the performance of this scheme.

**Key words.** Conservation laws, Discontinuous Galerkin Method, High Order Methods, Stability

**Abstract.** This article considers a new discretization scheme for conservation laws. The discretization setting is based on a discontinuous Galerkin scheme in combination with an approximation space that contains high-order polynomial modes as well as piece-wise constant modes on a sub-grid. The high-order modes can continuously be suppressed with a penalty function that is based on a sensor which is intertwined with the approximation space. Numerical tests finally illustrate the performance of this scheme.

**1. Introduction.** While discontinuous Galerkin (DG) and related high-order methods [8] are getting sufficiently mature to handle realistic problems in many applications, there still exist challenging problems where state-of-the-art methods suffer from the lack of nonlinear stability and their high sensitivity to under-resolved features. This directly affects the solution of important problems involving shocks and turbulence models, but it has also turned out to be a problem for simpler problems such as laminar or inviscid flows, if the meshes are not well adapted to the solution fields. This lack of robustness is one of the main challenges remaining for the wide adoption of high-order methods.

Several approaches have been proposed to address the issue. One simple method is to calculate a sensor that identifies the elements in the shock region and reduce the degree of approximating polynomials [3, 6]. This is usually combined with  $h$ -adaptivity to better resolve the shocks [9], and it can be quite satisfactory in particular for steady-state problems. In recent refined versions, these ideas have been combined with sub-cell resolution schemes, either by a high-order/low-order duality on unstructured [15] and structured [27] grids, or a finite-volume a-posteriori correction of marked cells on structured [11, 28] and unstructured [10] grids. Another sophisticated class of approaches include limiting, for example based on weighted essentially non-oscillatory (WENO) concepts [13, 19, 17]. A related approach is to filter the solution in order to stabilize the discontinuities, see e.g. [5]. While these various schemes have been demonstrated to handle very strong shocks with no robustness issues, for various reasons they have not been widely employed to large-scale 3D problems on unstructured meshes, which typically require implicit solvers.

Alternatively, in [22] it was demonstrated how a strategy inspired by the early artificial viscosity methods can be very effective in the context of high-order DG methods. Based on the early stabilization proposed by Neumann [29] and used for discontinuous Galerkin methods in an element-wise way [2, 3, 14], the method combines a highly selective spectral sensor, based on orthogonal polynomials, with a consistently discretized artificial viscosity added to the equations. The goal is to smooth the discontinuities in the solution to a width that is appropriately resolved by the mesh and the polynomial approximations, which means in particular that the method obtains sub-cell resolution for high-order discretizations, which gives a number of important benefits. The continuous nature of the scheme allowed for Newton methods to produce fully converged solutions to steady-state problems or to implicit time-stepping problems. The method has been widely employed and improved, e.g. in [18, 1, 23]. A related class of schemes uses so-called physics-based sensors and viscosities [16, 4, 20]. Although popular, the artificial viscosity approaches still suffer from spurious oscillations and parameter sensitivities.

In the present work, we are proposing a new approach, based on a combination of the excellent

shock-capturing properties of the finite volume method and the high-order accuracy of the DG method. We define an approximation space that contains both, high-order polynomial modes and low-order piece-wise constant functions on a sub-grid, to design an approximation space. The fundamental idea is that the discontinuous Galerkin scheme, being a projection-based scheme, can use both modes for defining the approximation and the polynomial modes can be continuously suppressed by penalty if needed. Appropriate numerical dissipation is automatically introduced by the jumps of the solution. The penalty, which is based on a sensor function is a delicate issue. However, the richness of the approximation space allows for a powerful construction of such a sensor function which not only allows the detection of shocks but also indicates efficiently recovery in an element where penalization should be removed. Our approach is related to the contributions [15, 27, 11, 28, 10] referenced above involving a sub-grid as well. With exception of [15], these methods use a on/off-procedure to enable the (sub-grid) lower-order scheme based on an a posteriori approach for detection and reconstruction. While the method in [15] switches continuously between a low-order/high-order interpretation of the degrees of freedom we propose a combined approximation space and continuously suppress the high-order modes with a penalty function that arises naturally from the approximation space.

The outline of this article is as follows. The second section introduces the approximation space as well as several  $L^2$ -projections used within this framework. Section three considers space and time discretization of (generally non-linear) conservation laws and Section four presents various numerical results and tests in one and two spatial dimensions. Section five is devoted to some conclusions.

**2. The approximation space and its properties.** Here, we first introduce the approximation space and propose some basis functions considered within this framework. Further, we will introduce different projections that will be used in the following.

**2.1. Polynomials with sub-grid components.** Our approach is a standard discontinuous Galerkin method with a particular choice of approximation space. Consider a partition  $T = \{K_1, \dots, K_{N_T}\}$  of a domain  $\Omega \subset \mathbb{R}^d$ ,  $d \geq 1$ . Let  $h_K$  denote the diameter of the element  $K \in T$ . In each element  $K_\ell$ , we define a sub-grid  $T_{K_\ell} = \{k_1^\ell, \dots, k_n^\ell\}$  of size  $n$ . Note that  $n$  can in principle vary with  $\ell$ , this is however omitted for sake of a simple presentation. For a 1D line segment, this sub-grid could for example be a uniform partition of each element. Then, for each element  $K \in T$ , we first define the space of polynomials of at most degree  $p$  with zero average:

$$V_{\text{ho},p}(K) = \left\{ v \in \mathbb{P}_p(K) : \int_K v \, dx = 0 \right\}, \quad (2.1)$$

where  $\mathbb{P}_p(K)$  denotes a space of polynomials of total degree  $p$  on  $K$ , as well as the space of piece-wise constant functions in each element  $k$  on the sub-grid triangulation  $T_K$ :

$$V_{\text{o},n}(K) = \{v \in L_2(K) : v|_k \in \mathbb{P}_0(k) \, \forall k \in T_K\}. \quad (2.2)$$

Note that again, the polynomial degree  $p$  can also vary locally in the partition  $T$ . We then combine these spaces to obtain the approximation space that will be considered in this framework:

$$V_\delta(K) = V_{\text{ho},p}(K) \oplus V_{\text{o},n}(K). \quad (2.3)$$

Here, the two discretization parameters  $p$  and  $n$  are compactly denoted as  $\delta := (p, n)$ . We note that the condition on the integral of the functions in the polynomial space is necessary to avoid duplicating the constant function on  $K$ . Clearly, the space  $V_\delta(K)$  reproduces the DG and the FVM methods in the extreme cases:

- If the sub-grid equals the original element ( $n = 1$  and thus  $T_K = \{K\}$ ), the space is simply the polynomials of degree  $p$  and the resulting space is the standard DG space.
- If the polynomial degree is  $p = 0$ , the space consists of the piece-wise constant functions on the sub-grid and the resulting space is the standard space that is used for the FVM method.

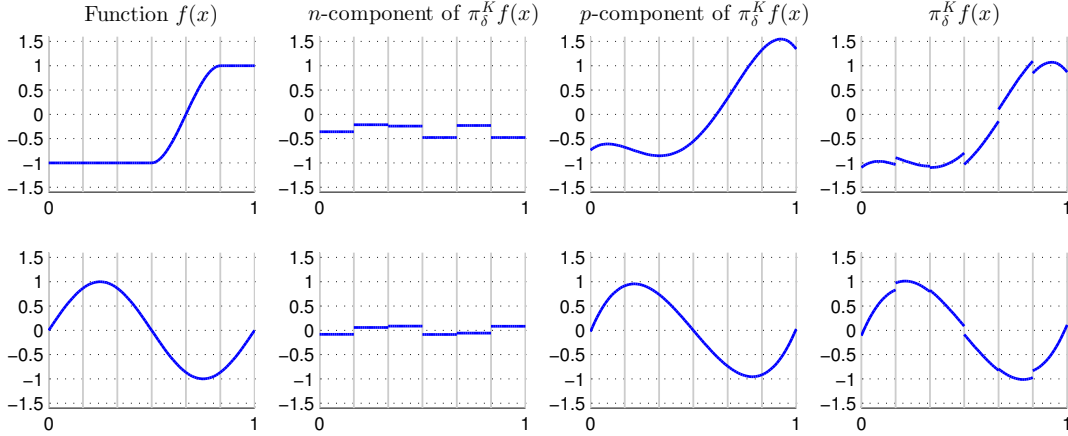


Fig. 2.1: Projection  $\pi_{\text{ho},p}^K f$  of two smooth example functions  $f$  on the space  $V_\delta(K)$  for  $p = 4$  and  $n = 6$  where the two components in  $V_{\text{lo},n}(K)$  and  $V_{\text{ho},p}(K)$  of  $\pi_{\text{ho},p}^K f$  are also indicated.

However, for a non-trivial combination of  $n$  and  $p$ , we obtain a new space with interesting properties. Discontinuities can be handled efficiently by the piece-wise constants, while the asymptotic high-order convergence rates for smooth solutions are obtained by the polynomials.

Finally, we now consider the global space given by

$$V_\delta = \bigoplus_{K \in T} V_\delta(K).$$

Therefore, any function  $v_\delta \in V_\delta$  lies locally in  $V_\delta(K)$ , i.e.  $v_\delta|_K \in V_\delta(K)$  for all  $K \in T$ .

**2.2. Basis functions.** Within each element  $K \in T$ , we introduce the following basis functions for the space  $V_\delta(K)$ . Let  $L_i^\ell$ ,  $i = 0, \dots, N(p)$  be a set of orthogonal polynomials up to total degree  $p$  on  $K_\ell$  such that  $L_0^\ell = 1$ . In one spatial dimension, we use the Legendre polynomials. Then, we define the following  $N(p) + n$  basis functions for  $V_\delta(K)$  by

$$\varphi_i^\ell = \begin{cases} L_i^\ell & i = 1, \dots, N(p), \\ \mathbb{1}_{k_j^\ell} & j = 1, \dots, n, i = N(p) + j, \end{cases} \quad (2.4)$$

where we use the characteristic function

$$\mathbb{1}_k(x) = \begin{cases} 1 & x \in k, \\ 0 & \text{otherwise.} \end{cases} \quad (2.5)$$

Note that while both, the polynomial components and the low order piece-wise constant components, are orthogonal w.r.t the  $L_2$ -norm, the combined basis is in general not orthogonal.

**2.3. Projections onto approximation spaces.** Let us first introduce three  $L^2$ -projections on the spaces we have defined. First, consider the projection  $\pi_{\text{ho},p}^K : L^2(K) \rightarrow V_{\text{ho},p}(K)$  on the polynomial modes: for any  $f \in L^2(K)$ , find  $\pi_p^K f \in V_{\text{ho},p}(K)$  such that

$$(\pi_{\text{ho},p}^K f, v_p)_K = (f, v_p)_K, \quad \forall v_p \in V_{\text{ho},p}(K). \quad (2.6)$$

Next, define the projection  $\pi_{\text{lo},n}^K : L^2(K) \rightarrow V_{\text{lo},n}(K)$  on the piecewise constant sub-grid space: for any  $f \in L^2(K)$ , find  $\pi_n^K f \in V_{\text{lo},n}(K)$  such that

$$(\pi_{\text{lo},n}^K f, v_n)_K = (f, v_n)_K, \quad \forall v_n \in V_{\text{lo},n}(K). \quad (2.7)$$

Finally, define the projection on the combined space  $\pi_\delta^K : L^2(K) \rightarrow V_\delta(K)$  given by: for any  $f \in L^2(K)$ , find  $\pi_\delta^K f \in V_\delta(K)$  such that

$$(\pi_\delta^K f, v_\delta)_K = (f, v_\delta)_K, \quad \forall v_\delta \in V_\delta(K). \quad (2.8)$$

Note that since the spaces  $V_{\text{ho},p}(K)$  and  $V_{\text{lo},n}(K)$  are in general not orthogonal with respect to  $L^2(K)$ , the projection  $\pi_\delta^K$  is not simply the sum of  $\pi_{\text{ho},p}^K$  and  $\pi_{\text{lo},n}^K$ . Also, all of these projections can be defined on the global spaces in a straight-forward way. The elementwise extension of  $\pi_\delta^K$  to  $\Omega$  is simply denoted by  $\pi_\delta$ . Figure 2.1 illustrate the projection of  $\pi_\delta^K f$  of two functions  $f$  as well as the components of  $\pi_\delta^K f$  lying in  $V_{\text{lo},n}(K)$  and  $V_{\text{ho},p}(K)$ .

Since the  $L^2$ -approximation is the best-approximation in the discrete space with respect to the  $L^2$ -norm and since the space  $V_\delta(K)$  contains the polynomial space  $\mathbb{P}_p(K)$  we obtain immediately the following estimate for the  $L^2$ -projection: Let  $f \in H^s(K)$ , then

$$\|f - \pi_\delta^K f\|_K \leq C \left( \frac{h_K}{p} \right)^s |f|_{H^s(K)}$$

for all  $1 \leq s \leq \min(p+1, k)$  for some constant  $C$  independent of  $h_K, p$  and  $n$ . Similar results can be obtained for other Sobolev norms of the error, see [25, 7]. Therefore, exponential convergence can be obtained for analytic solutions under  $p$ -refinement. On the other hand, since the space contains the piece-wise functions on the sub-grid  $T_K$ , one obtains the following estimate

$$\|f - \pi_\delta^K f\|_K \leq C \frac{h_K}{n} |f|_{H^1(K)}.$$

Finally, we note that  $\pi_\delta^K$  (and  $\pi_n^K$ ) preserves local averages on the sub-cells  $k_i^\ell$  since one can test in (2.8) with each sub-cell piece-wise constant basis function.

Figure 2.2 illustrates the  $L^2$ -projection of the Heaviside-function onto the considered approximation space, as well as the projection onto a pure polynomial space. As one can see, the presence of the piece-wise low order components does reduces the overshoot only for very (too) large  $n$ . However, in the asymptotic limit  $n \rightarrow \infty$  we have observed that the overshoots are reduced with a rate of  $1/n$  (the results are not reported here for the sake of compact presentation). Since this is not satisfactory, we explain in the next sub-section a strategy to project only on the low-order modes if necessary.

**2.4. Projections with penalized High-Order Components.** We note that the projections of monotonic functions on the  $V_\delta$ -space are in general not monotonic, which can cause severe problems for the solution of non-linear PDEs. Here, we propose a penalization approach in order to suppress the polynomial modes within elements flagged by an indicator function.

Given a constant element penalty parameter  $\gamma \geq 0$  (see the upcoming Section 2.5 for an explicit construction), we extend the projection (2.8) by adding a penalty term, to define the local penalized projection  $\pi_{\delta,\gamma}^K f$  of  $f$  in element  $K$  according to: for any  $f \in L^2(K)$ , find  $\pi_{\delta,\gamma}^K f \in V_\delta(K)$  such that

$$(\pi_{\delta,\gamma}^K f, v_\delta)_K + \gamma (\pi_p^K(\pi_{\delta,\gamma}^K f), \pi_p^K v_\delta)_K = (f, v_\delta)_K, \quad \forall v_\delta \in V_\delta(K). \quad (2.9)$$

This projection is well-defined since the bilinear form on the left hand side still defines a scalar product for any  $\gamma \geq 0$ . The motivation behind this projection is that the polynomial modes will be continuously suppressed for increasing values of  $\gamma$ . This can be easily seen from the equivalent minimization

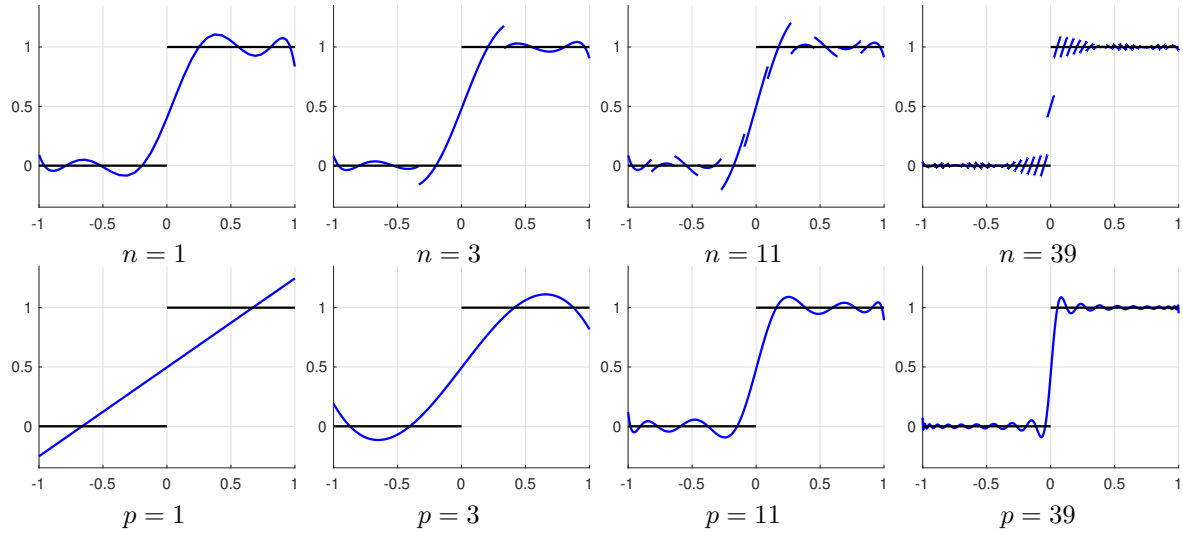


Fig. 2.2:  $L^2$ -approximation of a Heaviside-function using the approximation space  $V_\delta(K)$  introduced here with  $\delta = (p = 8, n)$  (top) and a polynomial approximation space (bottom), i.e.  $\delta = (p, n = 1)$ .

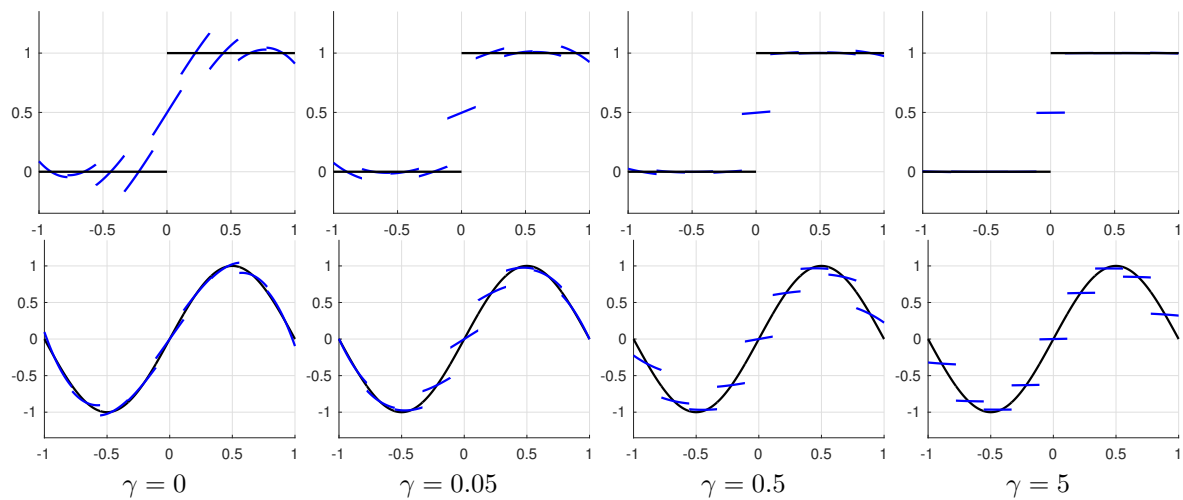


Fig. 2.3: Penalty-based  $L^2$ -projection ( $p = 4, n = 9$ ) for an increasing sequence of  $\gamma$  of the Heaviside-function (top) and the sin-function (bottom).

formulation for  $\pi_{\delta,\gamma}^K f$ :

$$\pi_{\delta,\gamma}^K f = \arg \min_{w_\delta \in V_\delta(K)} \left[ \|w_\delta - f\|_K^2 + \gamma \|\pi_p^K(w_\delta)\|_K^2 \right].$$

In Figure 2.3 we present the penalty-based  $L^2$ -projection for a sequence of increasing values of  $\gamma$  of the Heaviside-function as well as a smooth sin-function. As we can see, as is theoretically justified, the result converges to the monotonic  $L^2$ -projection using only the low-order modes.

**2.5. Indicator.** Having an indicator for the penalty-based  $L^2$ -projection at hand is an essential ingredient. A number of different sensors or indicators have been proposed in the literature, to identify so-called “trouble cells” where some kind of additional stabilization procedure is required to avoid oscillations in the solution. In our setting, we find it natural to define such an indicator directly in terms of the spaces and projectors we use.

In particular, we define a sensor function  $s_K$  that measures *the ability to represent a function  $u_\delta$  within an element  $K$  by a pure polynomial function while still maintaining the local average on the sub-cells*. Now, the pure polynomial function that we mention above could in practice be taken as the  $L^2$ -projection (2.6) onto  $\widehat{V}_p(K) := V_{\text{ho},p}(K) \oplus \text{span}\{1\}$ , i.e. where in addition  $V_{\text{ho},p}(K)$  is augmented with the constant functions in order to obtain the full polynomial space. However, this projection is not the best polynomial function that minimizes the local average of the original function. This motivates to introduce another projection  $\bar{\pi}_{p,n}^K : V_\delta(K) \rightarrow \widehat{V}_{\text{ho},p}(K)$  given by: for any  $u_\delta \in V_\delta(K)$ , find  $\bar{\pi}_{p,n}^K u_\delta \in \widehat{V}_{\text{ho},p}(K)$  such that

$$\langle \bar{\pi}_{p,n}^K u_\delta, v_p \rangle_K = \langle u_\delta, v_p \rangle_K, \quad \forall v_p \in \widehat{V}_{\text{ho},p}(K), \quad (2.10)$$

where  $\langle \cdot, \cdot \rangle_K$  is defined by

$$\langle w_\delta, v_\delta \rangle_K := (\pi_{\text{o},n}^K w_\delta, \pi_{\text{o},n}^K v_\delta)_K, \quad \forall w_\delta, v_\delta \in V_\delta(K).$$

Indeed, the projection  $\bar{\pi}_{p,n}^K u_\delta$  is the solution to the following minimization problem

$$\inf_{v_p \in \widehat{V}_{\text{ho},p}(K)} \|\pi_{\text{o},n}^K(u_\delta - v_p)\|_K.$$

Of course, this projection is in general not well-posed, in particular if  $N(p) + 1 > n$ , i.e. if there are more degrees of freedom than conditions so that uniqueness is not given.

**LEMMA 2.1.** *Consider a uniform partition of the unit simplex into  $n = (r + 1)^d$  simplices of edge-length  $1/(r + 1)$ . If  $r \geq p$ , then the mapping  $\pi_{\text{o},n}^K : \widehat{V}_{\text{ho},p}(K) \rightarrow V_{\text{o},n}(K)$  is injective.*

The proof is presented in the appendix.

**REMARK 2.1.** *Numerical results indicate that Lemma 2.1 does not provide a sharp condition on the solvability for large values of  $p$ . For example, for  $d = 2$  and  $p = 4$ , the mapping is injective even for  $r = 3$  which generates a sub-grid of 16 triangles whereas  $N(4) + 1 = 15$ . In practise, it is easy to check solvability on the unit simplex by numerical computation for any given parameters  $p$  and  $n$  in given dimension  $d$  once and for all.*

It is easy to see that the injectivity of  $\pi_{\text{o},n}^K : \widehat{V}_{\text{ho},p}(K) \rightarrow V_{\text{o},n}(K)$  implies that  $\|\pi_{\text{o},n}^K \cdot\|_K$  is a norm on  $V_{\text{ho},p}(K)$  and that the projection  $\bar{\pi}_{p,n}^K$  defined by (2.10) is in consequence uniquely determined.

Now, having clarified the well-posedness of the projection  $\bar{\pi}_{p,n}^K$ , we are now ready to state the indicator function

$$s_K = \|\pi_{\text{o},n}^K(u_\delta - \bar{\pi}_{p,n}^K u_\delta)\|_{\infty,K}, \quad (2.11)$$

with  $\|\cdot\|_{\infty,K}$  being the  $L^\infty(K)$ -norm. Therefore, the sensor  $s_K$  can be viewed as the maximal error if one would replace the current approximation  $u_\delta$  by the (pure) polynomial that best preserves the local averages on the sub-cells.

We also define a local normalization factor for this sensor, which is given by

$$s_K^0 = \|\pi_{\text{o},n}^K u_\delta\|_{\infty,K} + s_\varepsilon, \quad (2.12)$$

where  $s_\varepsilon$  is a small number to avoid zero division.

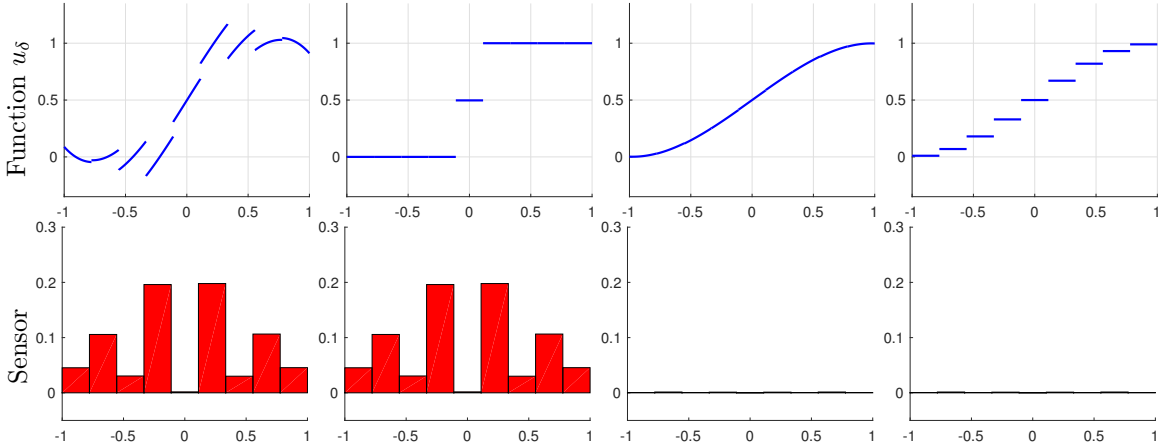


Fig. 2.4: Illustration of the sensor function  $|\pi_{10,n}^K(u_\delta - \pi_{p,n}^K u_\delta)|$  over one element  $K = (-1, 1)$  (bottom) for  $p = 4$ ,  $n = 9$  applied to four different functions (top).

In terms of this sensor  $s_K$ , we now define the penalty function

$$\gamma_K = C_{\text{pen}} \max \left( 0, \frac{s_K}{s_K^0} - \tau \right) \quad (2.13)$$

where  $C_{\text{pen}}$  is a problem and discretization dependent parameter, which we empirically set to  $C_{\text{pen}} = 10^7$  in all our examples. The threshold  $\tau$  is used to ensure zero penalization for smooth solutions and small perturbations, and we set it empirically to  $\tau = 0.01/p$ .

Figure 2.4 illustrates the sensor function  $|\pi_{10,n}^K(u_\delta - \pi_{p,n}^K u_\delta)|$  for four different functions using the discretization parameters  $p = 4$  and  $n = 9$ . We observe that the sensor indicates the first two functions as they can not be represented accurately by the  $L^2$ -projection onto polynomials only. We finalize this section with listing some properties of the sensor:

- If  $u_\delta \in \widehat{V}_{\text{ho},p}(K)$ , then  $s_K = 0$  since  $\pi_{p,n}^K u_\delta = u_\delta$ . Figure 2.4 (third column) illustrates this property: this function is a pure polynomial function (with  $p = 4$ ) so that  $\pi_{p,n}^K u_\delta = u_\delta$ . The relatively small error should not impact the sensor which motivates a positive threshold parameter  $\tau = 0.01/p$ .
- If  $u_\delta \in V_{\text{lo},n}(K)$ , then  $s_K$  is in general positive. It can nevertheless be zero or very small if the function can be nicely represented by a polynomial while keeping the local averages in the sub-cells, which is an important feature to allow for recovering the high-order representation, e.g. after a shock-transition. This is illustrated in Figure 2.4 (fourth column) which does not sense this function (although it is a piecewise constant function).

**3. Discontinuous Galerkin formulation for conservation laws.** We devote now our attention to the discretization of conservation laws using the previously introduced approximation space  $V_\delta$ .

**3.1. Governing equations.** Consider a general system of first-order conservation laws

$$\frac{\partial u}{\partial t} + \nabla \cdot F(u) = 0 \quad \text{in } \Omega, \quad (3.1)$$

with prescribed initial condition  $u(x, t = 0) = u_0$  and appropriate boundary conditions on  $\partial\Omega$  (more details will be provided in the results section). Here  $u = (u_1, \dots, u_m)$  is the solution vector function and we will consider the following equation:

- [1] **Convection:** We consider  $m = 1$  and  $F(u) = \beta u$  for a given velocity field  $\beta$  (possibly space and time varying).
- [2] **Inviscid Burgers' equation:** The spatial dimension is limited to  $d = 1$  only; with  $m = 1$  and  $F(u) = u^2/2$ .
- [3] **Euler's equations of gas dynamics:** Here,  $m = d + 2$  and the system of conservation laws is given by

$$\frac{\partial \rho}{\partial t} + \frac{\partial}{\partial x_i}(\rho u_i) = 0, \quad (3.2)$$

$$\frac{\partial}{\partial t}(\rho u_i) + \frac{\partial}{\partial x_i}(\rho u_i u_j + p) = 0 \quad \text{for } i = 1, 2, 3, \quad (3.3)$$

$$\frac{\partial}{\partial t}(\rho E) + \frac{\partial}{\partial x_i}(u_j(\rho E + p)) = 0 \quad (3.4)$$

where  $u_i$ ,  $i = 1, \dots, d$  are the velocity components,  $\rho$  is the fluid density and  $E$  is the total energy, thus the unknown vector function consists of  $u = (u_1, u_2, u_3, \rho, E)$ . Further, we assume an ideal gas with pressure  $p$  of the form

$$p = (\gamma_a - 1)\rho \left( E - \frac{1}{2}u_k u_k \right), \quad (3.5)$$

where  $\gamma_a$  is the adiabatic gas constant.

**3.2. Spatial Discretization.** Our discretization is a standard (discontinuous) Galerkin form on our space  $V_\delta$ , with the optional penalization of the polynomial modes as described above. Define the multi-component spaces  $V_\delta^m(K) = [V_\delta(K)]^m$  and  $V_\delta^m = [V_\delta]^m$ . For all  $t \in (0, T)$ , find  $u_\delta(t) = (u_{\delta,1}(t), \dots, u_{\delta,m}(t)) \in V_\delta^m$  such that

$$\begin{aligned} \int_K \partial_t u_\delta(t) v_\delta - \sum_{k \in T_K} \int_k F(u_\delta(t)) \cdot \nabla v_\delta + \sum_{k \in T_K} \oint_{\partial k} \widehat{F}(u_\delta^+(t), u_\delta^-(t), n_k) v_\delta \\ + \gamma_K(u_\delta(t)) \int_K (\pi_{\text{ho},p}^K u_\delta(t)) (\pi_{\text{ho},p}^K v_\delta) = 0, \quad \forall v_\delta \in V_\delta^m(K), \end{aligned} \quad (3.6)$$

on each element  $K \in T$ . We are using a compact notation to handle the multi-component system. Here,  $\widehat{F}(u_\delta^+(t), u_\delta^-(t), n_k)$  is a numerical flux function involving the solution on each side of the boundary  $\partial k$  and the outward normal vector  $n_k$ .

Next, write the global  $u_\delta$  approximation in terms of the basis functions  $\phi_i$ :

$$u_\delta(t) = \sum_{\ell=1}^{N_T} \sum_{i=1}^{N(p)+n} U_i^\ell(t) \varphi_i^\ell \quad (3.7)$$

where  $U$  is the vector of all components  $U_i^\ell = (U_{i,1}^\ell, \dots, U_{i,m}^\ell)$ ,  $\ell = 1, \dots, N_T$ ,  $i = 1, \dots, N(p) + n$ . Note that the dimension of  $U$  is  $m \times N_T \times (N(p) + n)$ . Imposing equation (3.7) for each basis function leads to a semi-discrete system of the form

$$M \dot{U}(t) + \Gamma(U(t)) M_{pp} U(t) = R(U(t)) \quad (3.8)$$

Here,  $M$  is a block-diagonal mass matrix,  $M_{pp}$  is a (singular) block-diagonal mass matrix for the polynomial components only,  $\Gamma(U(t))$  is a diagonal matrix with the values of the penalty parameter  $\gamma_K$  for each element, and  $R(U(t))$  contains the remaining terms (which is in general non-linear).

The initial condition, denoted by  $U_0$ , is obtained by projecting the initial function  $u_0$  onto the discretization space  $V_\delta$ .



**3.3. Time integration by Implicit-Explicit Runge-Kutta methods.** The system (3.8) can be integrated by a number of different ODE solvers, including fully implicit and fully explicit or combined implicit-explicit (IMEX) schemes. Since the penalty term  $\Gamma(U(t)) M_{pp} U(t)$  is very stiff we apply an IMEX scheme using the splitting

$$M\dot{U}(t) = f(U(t)) + g(U(t)),$$

with explicit part  $f$  and implicit part  $g$  given respectively by

$$f(U(t)) = R(U(t)), \quad g(U(t)) = -\Gamma(U(t)) M_{pp} U(t).$$

In particular, we use the approach presented in [23] where we freeze however the penalty function  $\Gamma$  during the different stages. One time-step from  $U_n \approx U(t^n)$  to  $U_{n+1} \approx U(t^{n+1})$  reads as:

```

Set  $\Gamma_n = \Gamma(U_n)$ 
for  $i = 1$  to  $s$ 
     $U_{n,i} = U_n + \Delta t \sum_{j=1}^{i-1} [a_{i,j} r_j + \hat{a}_{i,j} \hat{r}_j]$ 
    Evaluate  $(M + \Delta t a_{i,i} \Gamma_n M_{pp}) r_i = -\Gamma_n M_{pp} U_{n,i}$ 
    Evaluate  $M \hat{r}_i = R(U_{n,i} + \Delta t a_{i,i} r_i)$ 
end for
 $U_{n+1} = U_n + \Delta t \sum_{i=1}^s [b_i r_i + \hat{b}_i \hat{r}_i]$ .

```

We use the ARS(2,2,2) scheme, with coefficients  $a_{i,j}$ ,  $\hat{a}_{i,j}$ ,  $b_j$ ,  $\hat{b}_j$  given by the matrices  $A$ ,  $\hat{A}$  and vector  $b$ ,  $\hat{b}$ :

$$A = \begin{pmatrix} 0 & 0 & 0 \\ 0 & \alpha & 0 \\ 0 & 1 - \alpha & \alpha \end{pmatrix} \quad \hat{A} = \begin{pmatrix} 0 & 0 & 0 \\ \alpha & 0 & 0 \\ \delta & 1 - \delta & 0 \end{pmatrix} \quad b = \hat{b} = \begin{pmatrix} 0 \\ 1 - \alpha \\ \alpha \end{pmatrix},$$

with fixed parameters  $\alpha = 1 - \frac{1}{\sqrt{2}}$ ,  $\delta = -2\frac{\sqrt{2}}{3}$ .

**4. Results.** We present here a collection of numerical results in one and two spatial dimensions with increasing complexity. We use Roe's approximate Riemann solver for the numerical flux function in all our examples.

**4.1. Linear convection.** We start with the most simple case of scalar linear convection in one spatial dimension, see Section 3.1 [1] with  $\beta = 1$ , on  $\Omega = (0, 1)$  in order to illustrate some basic approximation properties. We consider two initial conditions  $u_0 = u(t = 0)$ , a Gaussian function and a Heaviside function, that are evolved under periodic boundary conditions for one cycle to obtain  $u_\delta(t = 1)$ . The polynomial degree  $p = 1, 2, 3, 4$  and the number of sub-cells  $n = 8$  per element is fixed while the number of elements  $N_T$  is increased to generate convergence rates as  $h \rightarrow 0$  where  $h = 1/n_T$  denotes the diameter of the elements. The time-step  $\Delta t$  is kept small enough so that the error is dominated by the spatial discretization.

In Figure 4.1 (left) we illustrate the  $L^2(\Omega)$ -norm of the error  $\pi_\delta u_0 - u_\delta(t = 1)$  for the different values of  $p$  under mesh-refinement  $h \rightarrow 0$  for the Gaussian function while 4.1 (right) plots the same errors in the  $L^1(\Omega)$ -norm, which is standard for discontinuous solutions, for the Heaviside function.

Finally, in Figure 4.2 we activate artificially the penalty parameter in one element and plot the solution of the transported Gaussian before, during and after it passes this element. We observe that the solution can qualitatively be recovered with the polynomial modes after the Gaussian traveled through the marked element, but that the shape suffers from the high dissipation that occurred during the piecewise constant representation in the marked element.

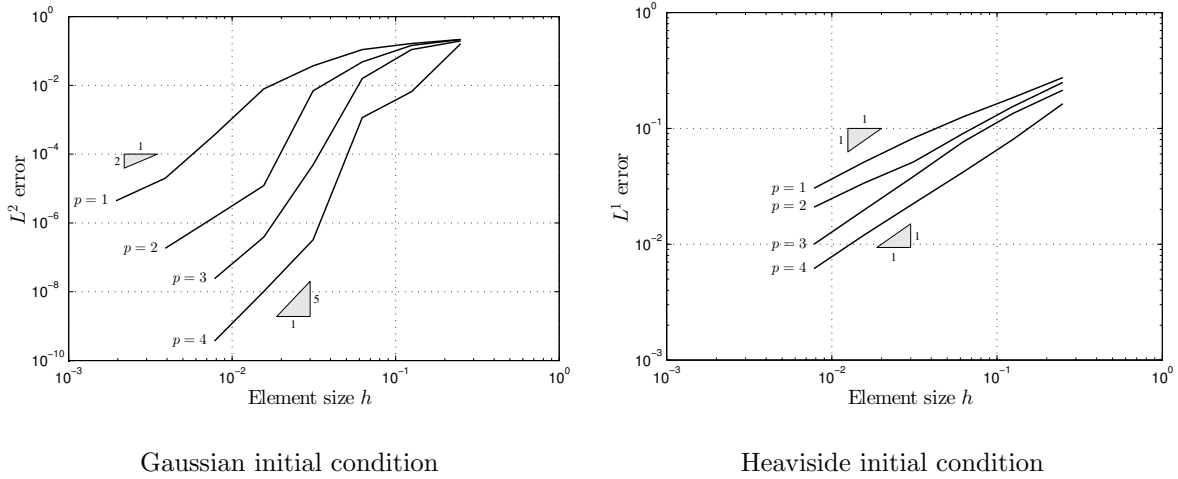


Fig. 4.1: Accuracy of the method for linear convection for a Gaussian (left) and Heaviside (right) initial condition with  $p = 1, 2, 3, 4$  and  $n = 8$  under mesh refinement at  $t = 1$ .

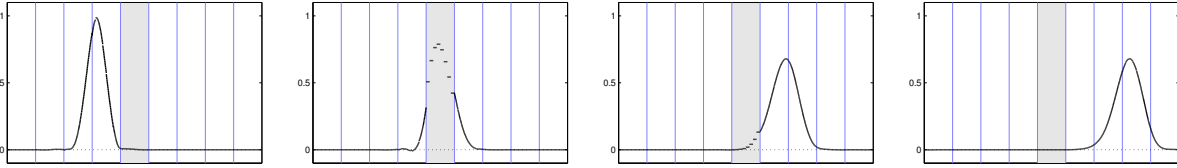


Fig. 4.2: Solution before, during and after it passes the marked element in which the penalization parameter is artificially activated.

**4.2. Inviscid Burgers' equation.** We now consider the inviscid Burgers' equation, see Section 3.1 [2], on  $\Omega = (0, 1)$  with smooth initial condition  $u_0(x) = 1/2 + \sin(2\pi x)$ . We illustrate in Figure 4.3 the solution and the indicator  $\gamma$  with  $p = 4$ ,  $n = 8$  on  $n_T = 9$  elements at various times. The time-step is set to  $\Delta t = 10^{-3}$ . We observe that the indicator starts to be activated when the strong gradient appears even before the shock is formed since a polynomial representation with  $p = 4$  of the solution would yield oscillations. Second, it also can be seen that the indicator can deal with the moving shock and that the solution is recovered in polynomial representation after the shock left an element. We also note that the standard discontinuous Galerkin method with high order elements will not lead to an approximation since over- and undershoots are amplified and the simulation aborted.

**4.3. Transonic Quasi-1D flow through nozzle.** We now shed our attention to a nozzle flow-problem under quasi-1D assumptions. The resulting equations are similar to the one-dimensional Euler equations, see Section 3.1 [3], with minor modifications. For the variable-area  $A(x)$ , this leads to the

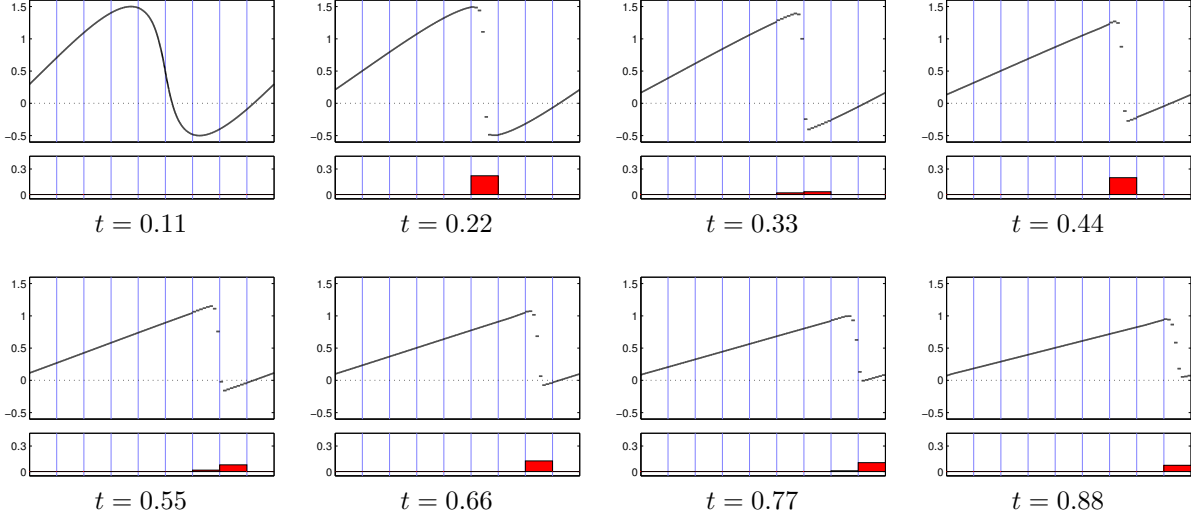


Fig. 4.3: Evolution of the solution to the inviscid Burgers' with  $p = 4$ ,  $n = 8$  and  $n_T = 9$  elements at various times.

equations

$$\begin{aligned}
 \frac{\partial}{\partial x}(A\rho u) &= 0, \\
 \frac{\partial}{\partial x}(A[\rho u^2 + p]) &= \frac{p}{A} \frac{\partial A}{\partial x}, \\
 \frac{\partial}{\partial x}(A[\rho E + p]u) &= 0
 \end{aligned} \tag{4.1}$$

where  $\rho$  is the fluid density,  $u$  is the fluid velocity, and  $p$  is the thermodynamic pressure. The total energy is given by  $\rho E = \rho e + \rho u^2/2$ , and the pressure is related to  $\rho E$  by the equation of state for a perfect gas,  $p = (\gamma_a - 1)(\rho E - \rho u^2/2)$ , where the ratio of specific heats  $\gamma_a = 1.4$ . The Mach number is the ratio between the speed of the flow and the speed of sound  $M = u/c$ , where  $c = \sqrt{\gamma_a p/\rho}$ .

We solve on the domain  $\Omega = (0, 1)$ , and prescribe the nozzle area by

$$A(x) = \begin{cases} 1 - (1 - T_n) \cos\left(\pi \frac{x-0.5}{0.8}\right)^2 & \text{for } 0.1 \leq x \leq 0.9 \\ 1 & \text{otherwise,} \end{cases} \tag{4.2}$$

where  $T_n = 0.8$  is the height of the nozzle throat. At  $x = 0$  we impose the farfield conditions  $\rho = \rho_i = 1.0$ ,  $u = u_i = 1.0$ ,  $M = M_i = 0.40$  weakly, and at  $x = 1$  we impose the conditions  $\rho = \rho_o = 1.0$ ,  $u = u_o = 1.0$ ,  $M = M_o = 0.45$ .

This problem is a challenging problem for high-order methods since small densities occur and thus small undershoots lead to very large relative undershoots. Figure 4.4 presents the first solution component  $A\rho$  at various times with  $p = 4$ ,  $n = 8$  on  $n_T = 9$  elements. The time-step is set to  $\Delta t = 2 \cdot 10^{-4}$ . We observe that the steady-state is reached and that the indicator is activated in the element containing the shock.

**4.4. The Shu-Osher Shock Tube Problem.** Next we model the Shu-Osher problem [26], which consists of a shock front moving inside a one-dimensional inviscid flow with artificial density fluctuations.

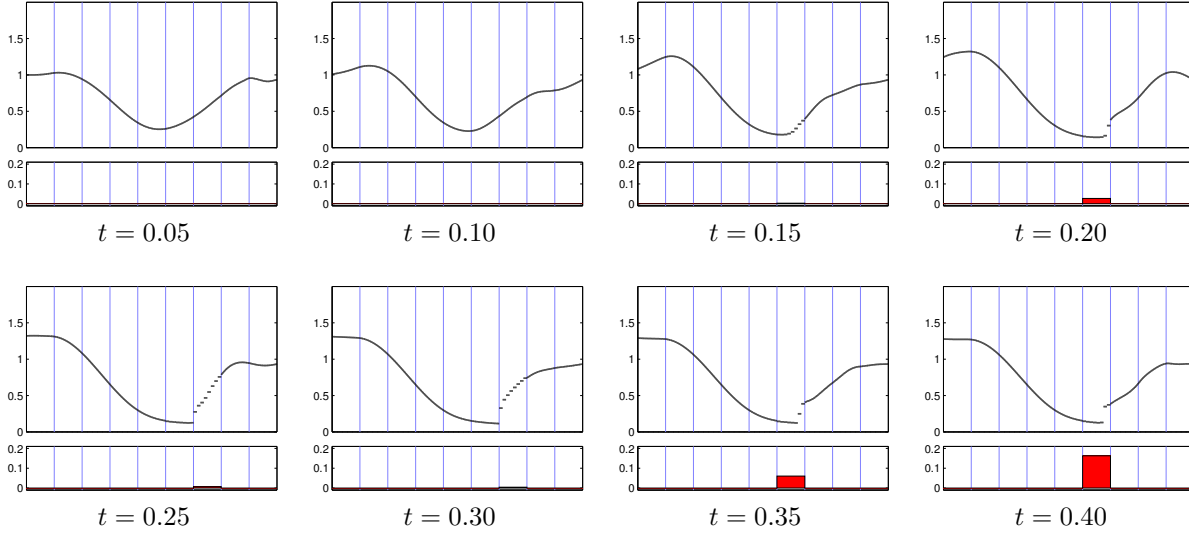


Fig. 4.4: Transonic flow through a quasi-1D nozzle. The plots show the weighted density  $A\rho(x)$  at various times. Discretized using  $p = 4$  and  $n = 8$ . Note the sharp resolution of the shock on the sub-grid.

The governing equations are the 1D compressible Euler equations for an ideal gas with a constant ratio of specific heats equal to  $\gamma = 1.4$ . The flow domain is  $\Omega = (-5, 5)$  and the time domain is  $(0, T)$  with  $T = 1.78$ . The initial condition for the flow is

$$(\rho, u, p) = \begin{cases} (3.857143, 2.629369, 10.3333) & x < -4 \\ (1 + 0.2 \sin(5x), 0, 1) & x \geq -4 \end{cases} \quad (4.3)$$

with a supersonic inlet at  $x = -5$  that prescribes the density, velocity, and pressure  $(\rho, u, p) = (3.857143, 2.629369, 10.3333)$  and a solid wall at  $x = 5$ . This problem corresponds to a Mach  $M = 3$  shock moving into a field with a small density (or entropy) disturbance.

We solve the problem for polynomial degrees  $p = 1, 2, 3$  on two different uniform grids, with  $n_T = 64$  and  $n_T = 256$  elements, respectively. In all cases, we set the sub-grid size to  $n = p + 2$ . The timestep is chosen small enough that temporal errors are negligible.

The resulting density fields are shown in Figure 4.5, together with a reference solution (computed using a WENO scheme on a very fine grid). We observe that the method generates stable solutions for all cases, and that the accuracy of the scheme increases substantially for higher polynomial degrees  $p$ .

**4.5. Euler Vortex.** Our first 2D example is the inviscid flow of a compressible vortex in a rectangular domain [12]. The vortex is initially centered at  $(x_0, y_0)$  and is moving with the free-stream at an angle  $\theta$  with respect to the  $x$ -axis. The analytic solution at  $(x, y, t)$  is given by

$$u = u_\infty \left( \cos \theta - \frac{\epsilon((y - y_0) - \bar{v}t)}{2\pi r_c} \exp(f/2) \right), \quad \rho = \rho_\infty \left( 1 - \frac{\epsilon^2(\gamma - 1)M_\infty^2}{8\pi^2} \exp(f) \right)^{\frac{1}{\gamma-1}}, \quad (4.4)$$

$$v = u_\infty \left( \sin \theta + \frac{\epsilon((x - x_0) - \bar{u}t)}{2\pi r_c} \exp(f/2) \right), \quad p = p_\infty \left( 1 - \frac{\epsilon^2(\gamma - 1)M_\infty^2}{8\pi^2} \exp(f) \right)^{\frac{\gamma}{\gamma-1}}, \quad (4.5)$$

where  $f(x, y, t) = (1 - ((x - x_0) - \bar{u}t)^2 - ((y - y_0) - \bar{v}t)^2)/r_c^2$ ,  $M_\infty$  is the Mach number,  $\gamma = c_p/c_v = 1.4$ , and  $u_\infty, p_\infty, \rho_\infty$  are free-stream velocity, pressure, and density. The Cartesian components of the

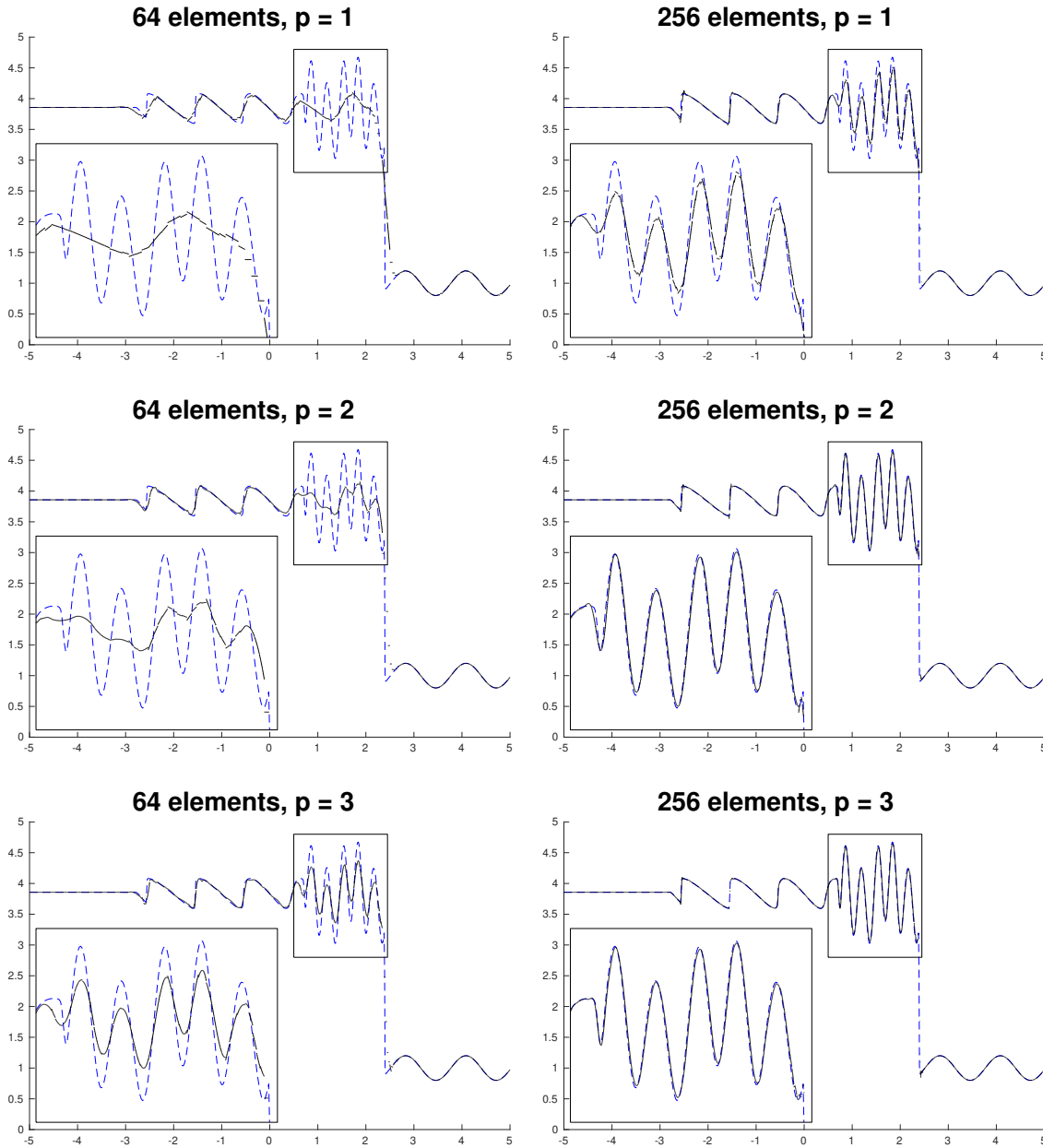


Fig. 4.5: The Shu-Osher Shock Tube problem. The plots show the density  $\rho(x)$  at the final time  $t = 1.8$ . Discretized using  $p = 1, 2, 3$  and  $n = p + 2$ . The reference solutions is shown in blue dashed line.

free-stream velocity are  $\bar{u} = u_\infty \cos \theta$  and  $\bar{v} = u_\infty \sin \theta$ . The parameter  $\epsilon$  measures the strength of the vortex and  $r_c$  is its size.

We use a domain of size 20-by-15, with the vortex initially centered at  $(x_0, y_0) = (5, 5)$  with respect to the lower-left corner. The Mach number is  $M_\infty = 0.5$ , the angle  $\theta = \arctan 1/2$ , and the vortex has the parameters  $\epsilon = 10$  and  $r_c = 1.5$ . We use characteristic boundary conditions and integrate until time

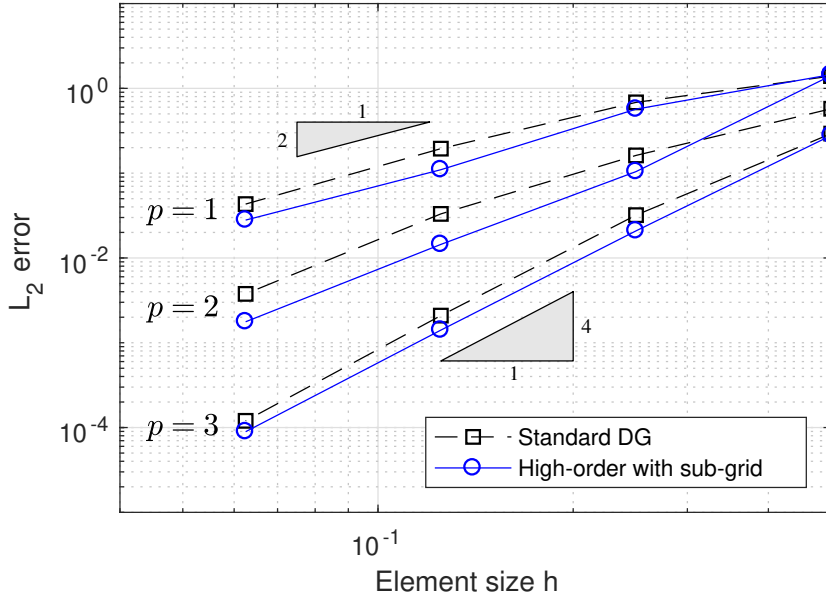


Fig. 4.6: Convergence test for an Euler vortex test problem using a standard DG method and our proposed mixed high- and low-order scheme. The results show optimal order of convergence  $\mathcal{O}(h^{p+1})$  for both methods. In general, the mixed scheme is more accurate than standard DG, since its approximation space is richer.

$t_0 = \sqrt{10^2 + 5^2}/10$ , when the vortex has moved a relative distance of  $(1, 1/2)$ .

In Figure 4.6, we graph the  $L_2$ -errors for all simulation cases, both for the standard DG method and our proposed method with a range of mesh sizes  $h$  and polynomial degrees  $p$ . The results clearly show the optimal order of convergence  $\mathcal{O}(h^{p+1})$  for both methods. The new method is slightly more accurate, which is expected since its approximation space is richer but contains the standard DG polynomials.

**4.6. The Woodward-Colella forward facing step.** We finally apply our method to the forward facing step problem of Woodward and Colella [30], in the context of Euler’s equations in two dimensions. The freestream Mach number is 3, and we discretize the high-order space using polynomials of degree  $p = 3$ , and create a sub-grid by refining each triangle into  $n = 4^2 = 16$  sub-cells uniformly. We integrate in time using a stepsize of  $\Delta t = 2 \cdot 10^{-4}$  until a final time 5.0. We only use a first-order accurate IMEX scheme in time, since our goal is to compute a steady-state solution which can be used to assess the shock capturing capabilities. The solution never reaches a steady-state due to transient effects and instabilities, but it serves as a good test case.

Figure 4.7 shows the results on a coarse and on a finer mesh, visualized by a density plot as well as the sensor and the mesh. First, we note that our sensor is highly selective and that only a single element layer of elements needs to be flagged for stabilization. The singularity at the convex corner causes some problems, as the oscillations due to under-resolution are convected downstream and results in an entire layer of elements along the wall being flagged by the sensor. This could likely be avoided by a finer resolution at the corner (as in [23]), different parameters for the sensor, or by special treatment of the corner as in the original work [30]. We also note numerical oscillations behind the shocks, in particular for the coarse mesh. This is due to the low-order finite volume scheme and known as the “carbuncle effect” [24], which can be remedied using a wide range of techniques [21].

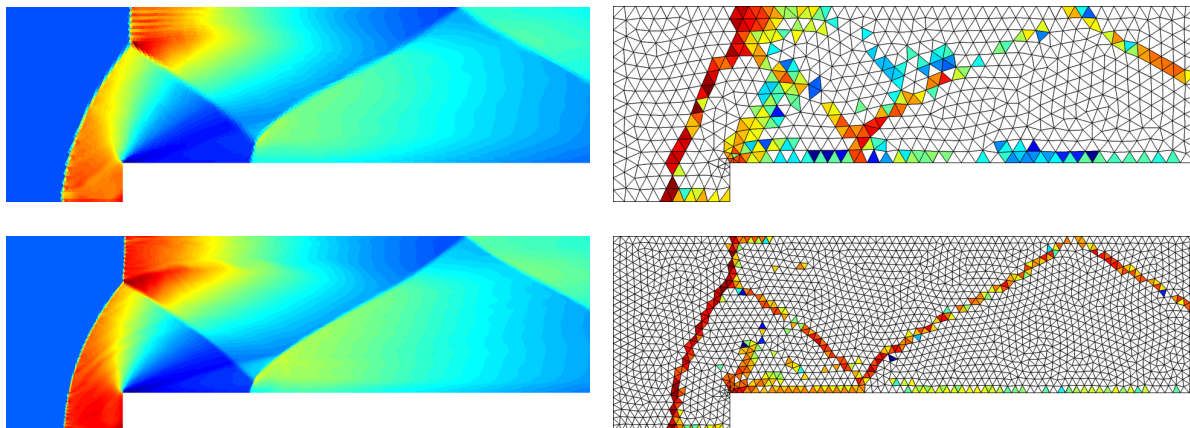


Fig. 4.7: The Woodward-Colella forward facing step problem [30]. The problem is discretized on a coarse mesh (top) and on a finer mesh (bottom), using polynomial degrees  $p = 3$  and a sub-grid of  $n = 4^2 = 16$  sub-cells in each triangle. The plots show the density (left) and the sensor on the mesh (right). In the sensor plots, gray color indicated no stabilization is applied. Note that most of the shocks are captured using only a single layer of low-order elements. The numerical oscillations are due to the low-order scheme (the so-called “carbuncle effect”, [24, 21]).

**4.7. Comparison with other methods.** Although it is difficult to draw conclusions about how our proposed high-order with sub-grid scheme compares to other methods, we can still illustrate how the solutions behave qualitatively and give some comments about the computational cost of the method.

In Figure 4.8, we show the Shu-Osher shock tube problem introduced earlier, using both the new sub-grid scheme and a standard DG scheme with the artificial viscosity stabilization proposed in [23, 22]. The amount of viscosity is chosen as small as possible to give stable solutions. Still, the sub-grid method gives much less numerical dissipation as well as a sharper shock profile.

To illustrate the benefits of the high-order accuracy, we also compare the with a standard cell-centered finite volume scheme in Figure 4.9. The grid is the same as the sub-grid used for the new method, that is, it corresponds to setting  $p = 0$  in our sub-grid method. The finite volume solution is highly inaccurate, in particular in the oscillatory region behind the shock, showing the benefit of the high-order polynomial modes.

Finally, we make some comments on the performance of our proposed scheme. Our implementation is only a prototype code, so wall-clock time comparisons with highly optimized codes would not give a accurate view of the actual computational cost. Instead, let us just comment on some of the main considerations:

**Degrees of freedom:** Clearly, the high-order with sub-grid method that we propose uses more degrees of freedom than a corresponding standard DG method on the same grid. More precisely, it needs  $n$  more degrees of freedom per solution component and element. Since we choose the number of sub-grid elements  $n$  approximately the same as the number of high-order DG coefficients, this ends up being about twice the number of degrees of freedom. However, note from the convergence plot in Figure 4.6 that these extra degrees of freedom also result in a more accurate solution.

**Computational cost of residual assembly:** Our implementation uses a standard DG code to compute all the integrals on the sub-grid, which is clearly inefficient since it assumes full polynomial degrees  $p$  everywhere (i.e. even on the sub-grid). This can easily be improved in a specialized code for the proposed sub-grid scheme. However, an important decision is how to compute the

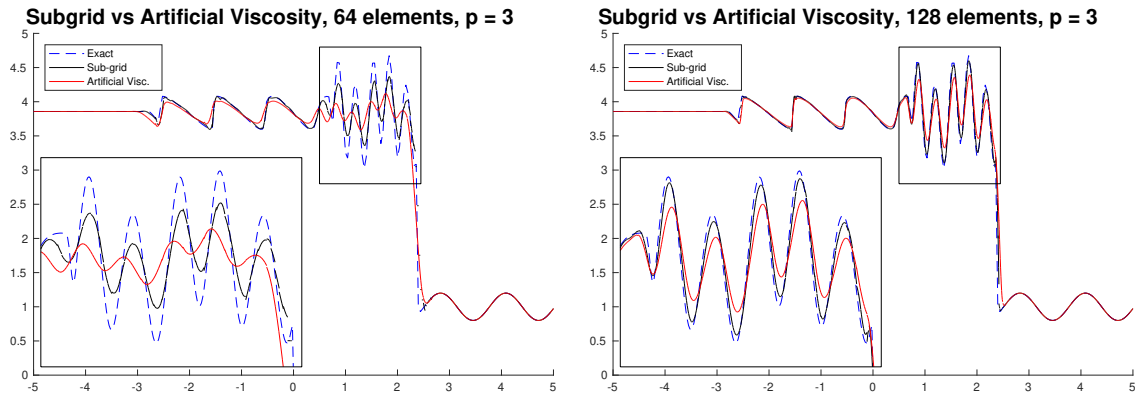


Fig. 4.8: Comparison between the high-order with sub-grid method and standard DG with artificial viscosity shock capturing [23, 22], for the Shu-Osher shock tube problem.

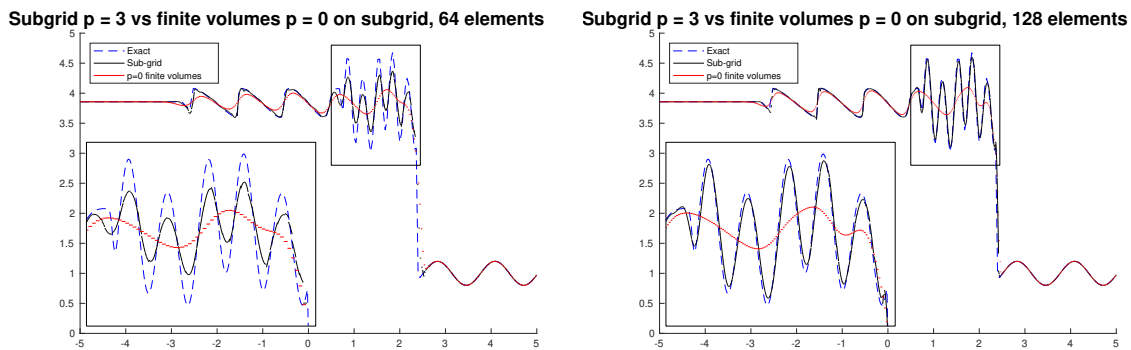


Fig. 4.9: Comparison between the high-order with sub-grid method and cell-centered 1st order finite volumes (standard DG with  $p = 0$ ) on the sub-grid, for the Shu-Osher shock tube problem.

integrals. The most straight-forward way is to use a high-order quadrature rule inside each sub-grid element and on the edges between them, which results in about  $n$  times as many quadrature points as standard DG. Future work includes the development of specialized quadrature rules for our particular solution spaces.

**Adaptive assembly of elements with shocks:** Typically, the high-order with sub-grid shock capturing scheme is only active in a small fraction of the mesh elements. Therefore, an obvious way to improve the performance of the method is to adaptively only apply the new scheme in those elements. This might need a more efficient shock indicator than the one we propose here, for example the resolution based indicator in [22], to avoid having to assemble the sub-grid everywhere. This should in principle make the cost of our method comparable with standard DG for most practical problems.

**5. Conclusions.** In this article, we have introduced a new numerical scheme to solve non-linear conservation laws with a discontinuous Galerkin method based upon a non-standard (discontinuous) approximation space. This space includes on each element both high-order polynomials and piecewise constant functions on a sub-grid. The set-up of the method is very general so that it can be applied to unstructured meshes consisting of simplex elements in any dimension.



Since a Galerkin method is a projection method which minimizes the residual over the approximation space, we argue that the method intrinsically has a tendency to choose a good balance between using low- or high-order features of the approximation space. This, however, only reduces, but does not cure, the problem of overshooting which is fundamental for non-linear problems. The particular structure of the approximation space allows to define a sensor with some nice properties which allows to define a local penalty parameter that suppresses the high order modes whenever the sensor is activated in a smooth way. The method also allows for recovering a polynomial representation once a shock has quit an element, however with an accuracy that is reduced due to the temporary low-order representation of the solution.

Several numerical tests illustrate the characteristics of the method. From our prototypical implementation, it is difficult to guess how expensive the method really is. We judge it however satisfying that we obtain a qualitatively correct solution in regard that a typical high-order method crashes without any sort of shock-capturing and that the high-order modes are only suppressed locally where needed.

**6. Acknowledgement.** Financial support from the France-Berkeley Fund under the project-name “Sub-cell Limiting for Shock-capturing in High-Order Discontinuous Galerkin Methods” is acknowledged.

#### REFERENCES

- [1] Garrett Barter. *Shock capturing with PDE-based artificial viscosity for an adaptive, higher-order discontinuous Galerkin finite element method*. PhD thesis, M.I.T., June 2008.
- [2] Francesco Bassi and S. Rebay. Accurate 2D Euler computations by means of a high order discontinuous finite element method. In *Fourteenth International Conference on Numerical Methods in Fluid Dynamics*, pages 234–240. Springer, 1995.
- [3] C. E. Baumann and J. T. Oden. A discontinuous *hp* finite element method for the Euler and Navier-Stokes equations. *Int. J. Numer. Methods Fluids*, 31(1):79–95, 1999. Tenth International Conference on Finite Elements in Fluids (Tucson, AZ, 1998).
- [4] Ankit Bhagatwala and Sanjiva Lele. A modified artificial viscosity approach for compressible turbulence simulations. *Journal of Computational Physics*, 228(14):4965–4969, 2009.
- [5] Marvin Bohm, Sven Schermeng, Andrew R. Winters, Gregor J. Gassner, and Gustaaf B. Jacobs. Multi-element SIAC filter for shock capturing applied to high-order discontinuous Galerkin spectral element methods. *J. Sci. Comput.*, 81(2):820–844, 2019.
- [6] A. Burbeau, P. Sagaut, and Ch.-H. Bruneau. A problem-independent limiter for high-order Runge-Kutta discontinuous Galerkin methods. *Journal of Computational Physics*, 169(1):111–150, 2001.
- [7] C. Canuto, M. Y. Hussaini, A. Quarteroni, and T. A. Zang. *Spectral methods*. Scientific Computation. Springer-Verlag, Berlin, 2006. Fundamentals in single domains.
- [8] B. Cockburn and C.-W. Shu. Runge-Kutta discontinuous Galerkin methods for convection-dominated problems. *J. Sci. Comput.*, 16(3):173–261, 2001.
- [9] Alain Dervieux, David Leservoisier, Paul-Louis George, and Yves Coudière. About theoretical and practical impact of mesh adaptation on approximation of functions and PDE solutions. *International Journal for Numerical Methods in Fluids*, 43(5):507–516, 2003. ECCOMAS Computational Fluid Dynamics Conference, Part I (Swansea, 2001).
- [10] Michael Dumbser and Raphaël Loubère. A simple robust and accurate a posteriori sub-cell finite volume limiter for the discontinuous galerkin method on unstructured meshes. *Journal of Computational Physics*, 319:163–199, 2016.
- [11] Michael Dumbser, Olindo Zanotti, Raphaël Loubère, and Steven Diot. *A posteriori* subcell limiting of the discontinuous Galerkin finite element method for hyperbolic conservation laws. *J. Comput. Phys.*, 278:47–75, 2014.
- [12] G. Erlebacher, M. Y. Hussaini, and C.-W. Shu. Interaction of a shock with a longitudinal vortex. *J. Fluid Mech.*, 337:129–153, 1997.
- [13] Ami Harten, Björn Engquist, Stanley Osher, and Sukumar R. Chakravarthy. Uniformly high-order accurate essentially nonoscillatory schemes. III. *Journal of Computational Physics*, 71(2):231–303, 1987.
- [14] Ralf Hartmann and Paul Houston. Adaptive discontinuous Galerkin finite element methods for the compressible Euler equations. *Journal of Computational Physics*, 183(2):508–532, 2002.
- [15] A. Huerta, E. Casoni, and J. Peraire. A simple shock-capturing technique for high-order discontinuous Galerkin methods. *International Journal for Numerical Methods in Fluids*, 69(10):1614–1632, 2012.

- [16] Antony Jameson, W. Schmidt, and Eli Turkel. Numerical solution of the Euler equations by finite volume methods using Runge Kutta time stepping schemes. In *14th Fluid and Plasma Dynamics Conference*, 1981.
- [17] Guang-Shan Jiang and Chi-Wang Shu. Efficient implementation of weighted ENO schemes. *Journal of Computational Physics*, 126(1):202–228, 1996.
- [18] Andreas Klöckner, Tim Warburton, and Jan S. Hesthaven. Viscous shock capturing in a time-explicit discontinuous Galerkin method. *Mathematical Modelling of Natural Phenomena*, 6(3):57–83, 2011. arXiv:1102.3190.
- [19] Xu-Dong Liu, Stanley Osher, and Tony Chan. Weighted essentially non-oscillatory schemes. *Journal of Computational Physics*, 115(1):200–212, 1994.
- [20] David Moro-Ludena. *An adaptive high order Reynolds-averaged Navier-Stokes solver with transition prediction*. PhD thesis, M.I.T., December 2014.
- [21] Maurizio Pandolfi and Domenic D’Ambrosio. Numerical instabilities in upwind methods: analysis and cures for the “carbuncle” phenomenon. *J. Comput. Phys.*, 166(2):271–301, 2001.
- [22] P.-O. Persson and J. Peraire. Sub-cell shock capturing for discontinuous Galerkin methods. In *44th AIAA Aerospace Sciences Meeting and Exhibit, Reno, Nevada*, 2006. AIAA-2006-0112.
- [23] Per-Olof Persson. Shock capturing for high-order discontinuous Galerkin simulation of transient flow problems. In *21st AIAA Computational Fluid Dynamics Conference, San Diego, CA*, Jun 2013. AIAA-2013-3061.
- [24] James J. Quirk. A contribution to the great Riemann solver debate. In *Upwind and High-Resolution Schemes*, pages 550–569. Springer Berlin Heidelberg, Berlin, Heidelberg, 1997.
- [25] Ch. Schwab. *p- and hp-finite element methods*. Numerical Mathematics and Scientific Computation. The Clarendon Press, Oxford University Press, New York, 1998. Theory and applications in solid and fluid mechanics.
- [26] Chi-Wang Shu and Stanley Osher. Efficient implementation of essentially nonoscillatory shock-capturing schemes. II. *J. Comput. Phys.*, 83(1):32–78, 1989.
- [27] Matthias Sonntag and Claus-Dieter Munz. Efficient parallelization of a shock capturing for discontinuous galerkin methods using finite volume sub-cells. *Journal of Scientific Computing*, 70(3):1262–1289, 2017.
- [28] François Vilar. A posteriori correction of high-order discontinuous galerkin scheme through subcell finite volume formulation and flux reconstruction. *Journal of Computational Physics*, 387:245–279, 2019.
- [29] John Von Neumann and Robert Richtmyer. A method for the numerical calculation of hydrodynamic shocks. *Journal of Applied Physics*, 21:232–237, 1950.
- [30] Paul Woodward and Phillip Colella. The numerical simulation of two-dimensional fluid flow with strong shocks. *J. Comput. Phys.*, 54(1):115–173, 1984.

## 7. Appendix.

**7.1. Proof of Lemma 2.1.** We first introduce some appropriate notation. Consider the set of multi-indices of total degree  $p$  in  $d = 1, 2, 3$  dimensions given by

$$\mathbb{N}_p := \{\boldsymbol{\alpha} \in \mathbb{N}_0^d \mid |\boldsymbol{\alpha}| \leq p\},$$

where  $|\boldsymbol{\alpha}| = \sum_{i=1}^d \alpha_i$  and define

$$\mathbf{x}^\boldsymbol{\alpha} := \prod_{i=1}^d x_i^{\alpha_i}, \quad \binom{\boldsymbol{\alpha}}{\boldsymbol{\beta}} := \prod_{i=1}^d \binom{\alpha_i}{\beta_i}$$

for any monomial  $\mathbf{x} = (x_1, \dots, x_d) \in \mathbb{R}^d$ . Here, we assume that  $\binom{n}{k} = 0$  for any  $k > n$  so that  $\binom{\boldsymbol{\alpha}}{\boldsymbol{\beta}} = 0$  if there exists  $i$  such that  $\alpha_i < \beta_i$ . The corresponding space of  $d$ -variate polynomials of total degree at most  $p$  given by

$$\mathbb{P}_p := \text{span}\{\mathbf{x}^\boldsymbol{\alpha} \mid \boldsymbol{\alpha} \in \mathbb{N}_p\},$$

is of dimension  $\dim(\mathbb{P}_p) = \binom{p+d}{d}$  where the set of monomials  $\mathbf{x}^\boldsymbol{\alpha}$  consists of a basis.

We consider the case  $r = p$  since the result follows immediately from the case  $r = p$  for  $r > p$ . Without loss of generality, we scale the unit simplex by a factor  $p + 1$  and therefore introduce

$$S_p = \{\mathbf{x} \in \mathbb{R}^d \mid \forall i = 1, \dots, d : x_i \in [0, p + 1] \text{ and } |\mathbf{x}| \leq p + 1\}.$$

Then, the sub-grid is given by the uniform partition of  $S_p$  into  $(p + 1)^d$  simplices that are congruent to the unit simplex  $\hat{S} := S_0$ . Indeed,  $d!$  unit simplices fit into the unit cube in  $d$  dimensions. Further,

the cube  $[0, p+1]^d$  consists of  $(p+1)^d$  unit cubes which can be divided into  $d!(p+1)^d$  unit simplices. Among all these unit simplices, there are  $(p+1)^d$  unit simplices contained in  $S_p$ .

We consider the subset of simplices

$$S_\alpha = \{\hat{\mathbf{x}} + \alpha \mid \hat{\mathbf{x}} \in \hat{S}\}$$

generated by different  $\alpha \in \mathbb{N}_p$ . There are therefore also  $|\mathbb{N}_p| = \dim(\mathbb{P}_p)$  simplicies and they all belong to  $S_p$ . We then consider the matrix

$$A_{\alpha\beta} = \int_{S_\alpha} \mathbf{x}^\beta d\mathbf{x} = \int_{\hat{S}} (\hat{\mathbf{x}} + \alpha)^\beta d\hat{\mathbf{x}} = \sum_{\gamma \in \mathbb{N}_p} \binom{\beta}{\gamma} \alpha^\gamma \int_{\hat{S}} \hat{\mathbf{x}}^{\beta-\gamma} d\hat{\mathbf{x}} = \sum_{\gamma \in \mathbb{N}_p} \binom{\beta}{\gamma} \alpha^\gamma \mathbf{f}(\beta - \gamma)$$

for all  $\alpha, \beta \in \mathbb{N}_p$  and where  $\mathbf{f}(\alpha) = \int_{\hat{S}} \hat{\mathbf{x}}^\alpha d\hat{\mathbf{x}}$ . Here we have employed a change of variable from  $S_\alpha$  to  $\hat{S}$  and the binomial formula. Now, introduce the two additional matrices

$$M_{\alpha\beta} = \alpha^\beta, \quad \text{and} \quad B_{\alpha\beta} = \binom{\beta}{\alpha} \mathbf{f}(\beta - \alpha),$$

so that  $A = MB$ . The matrix  $M$  is indeed the interpolation matrix of the monomials  $\mathbf{x}^\beta$  on the grid  $\alpha \in \mathbb{N}_p$ , which is invertible. Second, the matrix  $B$  is upper triangular with constant and non-zero diagonal

$$B_{\alpha\alpha} = \binom{\alpha}{\alpha} \mathbf{f}(\mathbf{0}) = |\hat{S}|,$$

and thus also invertible. In turn,  $A$  is invertible.

Let us now conclude the proof. Indeed, we consider any polynomial  $v_p \in \mathbb{P}_p$  given by  $v_p(\mathbf{x}) = \sum_{\beta \in \mathbb{N}_p} v_\beta \mathbf{x}^\beta$  with  $v_\beta \in \mathbb{R}$ . We now assume that  $v_p$  has zero average on each sub-cell. Among those  $n = (p+1)^d$  sub-cells, we only consider the set  $S_\alpha$  with  $\alpha \in \mathbb{N}_p$  and the conditions become: for all  $\alpha \in \mathbb{N}_p$ , there holds

$$\int_{S_\alpha} v_p(\mathbf{x}) d\mathbf{x} = 0 \quad \Leftrightarrow \quad \sum_{\beta \in \mathbb{N}_p} v_\beta \int_{S_\alpha} \mathbf{x}^\beta d\mathbf{x} = \sum_{\beta \in \mathbb{N}_p} A_{\alpha\beta} v_\beta = 0.$$

Since  $A$  is invertible, it follows that  $v_\beta = 0$  for all  $\beta \in \mathbb{N}_p$  and the mapping  $\pi_{\text{lo},n}^K : \widehat{V}_{\text{ho},p}(K) \rightarrow V_{\text{lo},n}(K)$  is injective.